1

Models of Triboelectric Effect

1.1 Introduction

Contact electrification (CE) exists universally between any materials. It can be widely applied for energy harvesting [1, 2], electrostatic printing [3], etc., but may also cause electric breakdown in electronics and even fires [4, 5]. Understanding CE mechanisms will be of great significance to accurately control the surface charge level upon requirements of applications. Although CE has been discovered for more than 2600 years, its mechanism continues to elude the scientific community due to lack of proper systematic studies. Long-term debates exist on the charge carriers of CE: some scientists demonstrated the electron transfer dominant mechanism, while others favored material or ion transfer mechanism. An early study in 1980 by Lowell and Rose-Innes concluded CE mechanism between metal and dielectric as the electron transfer, with the surface states model proposed [6]. Through redox chemical reactions induced by triboelectric static charges, Bard et al. further confirmed electrons as charge carriers in CE [7–10]. The thermionic emission behaviors observed by Xu et al. indicated electron transfer dominant mechanism, with the electron-cloud-potential-well model developed [11–14]. Through atomic force microscopy (AFM) studies conducted by Lin et al., Zhou et al., and Li et al., further evidences were provided for CE on microscale to support electron transfer mechanism [15–17]. In the meanwhile, the transfer mechanisms by materials or ions were proposed by other scientists. Prof. Whitesides' group conducted a series of works on CE in ionic electrets from 2003 [18–21], concluding the ion transfer dominant mechanism with a model proposed. Prof. Grzybowski's group discovered the mosaic of surface charge generated by CE as attributed to material transfer [22–25]. Giuseppe Pezzotti and Šutka et al. attributed electrification as the output of bond cleavage and chemical changes at the molecular scale, implying ion/material transfer mechanism in CE [26, 27]. Therefore, to provide an answer to this millennium puzzle, further systematic studies are still required on CE in various material systems with well-designed methodology.

Triboelectric Nanogenerators: Technology, Applications, and Commercialization, First Edition.
Yunlong Zi, Hengyu Guo, Jie Wang, Chi Zhang, Xiangyu Chen, and Qing Zhao.

1.2 Thermionic Emission Method

A method to quantitatively investigate real-time charge transfer in CE via triboelectric nanogenerator (TENG) as a function of temperature was reported based on thermionic emission in 2018 [11]. The conventional metal–polymer or polymer–polymer structure of TENGs was not adopted in this study, mainly because polymers could not withstand at high temperatures. Here, two kinds of high-temperature-resistant contact-separation (CS) mode TENGs, a Ti-SiO_2 TENG and a Ti-Al_2O_3 TENG, were designed and fabricated, which were able to withstand a maximum temperature of 673 K and operate stably for a long period of time. Each TENG was placed in a heating cabinet, which could provide the desired temperature with an accuracy of ±5 K. The structure of the Ti-SiO_2 TENG is shown in Figure 1.1a. The charges increasingly accumulate with the CS operation of the TENG and then tend to balance at 293 K. It is worth noting that both the short-circuit charge transfer Q_{SC} (0.45 nC) and the open-circuit voltage V_{OC} (1.3 V) are rather low, which means that the CS Ti-SiO_2 TENG in the experiment can only generate limited charges during the CS operation. Thus, to investigate the influence of temperature on the tribocharges on the surfaces, SiO_2 was first rubbed

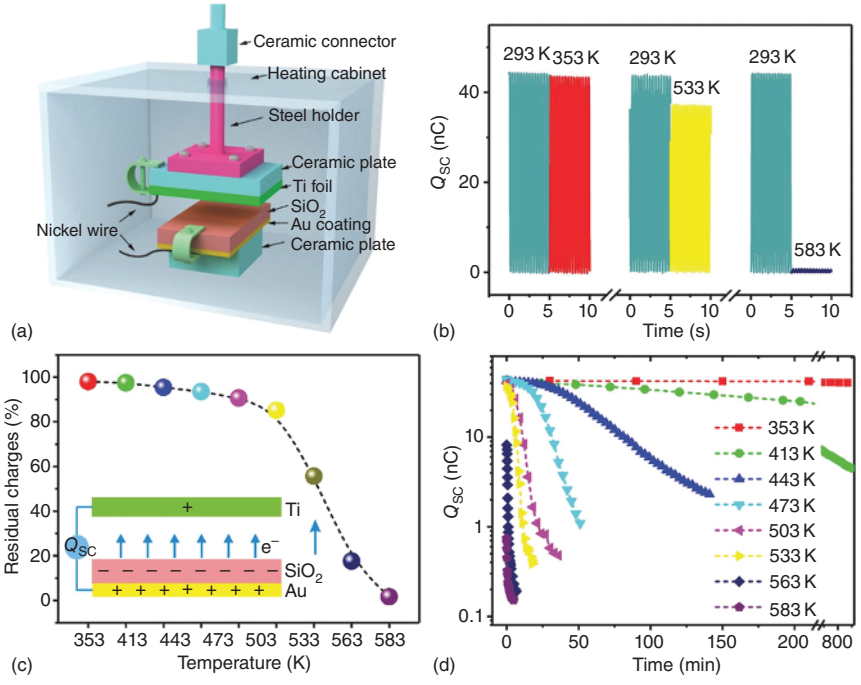

Figure 1.1 Performances of the Ti-SiO_2 TENG at different temperatures: (a) setup of the measurement platform, (b) the change of Q_{SC} at various temperatures, (c) the residual charges of the TENG at different temperatures (Inset is the diagram of the working model of the TENG) and (d) Q_{SC} evolution with time under high temperatures. Source: Reproduced with permission of [11], 2018 © John Wiley & Sons.

by polyurethane (PU) foam to introduce initial surface charges on SiO_2, as reflected by a Q_{SC} of around 45 nC. The cabinet was heated up to the desired temperature and then held for five minutes to measure the variation of Q_{SC}. Figure 1.1b shows the change of Q_{SC} at temperatures of 353, 533, and 583 K, demonstrating that the charge density decreased more rapidly at higher temperatures. When the temperature rose to 583 K, the charges quickly disappeared and the total charges Q_{SC} were less than 1 nC. Figure 1.1c shows the residual charges on the TENG after five minutes of measurement at different temperatures and the inset is the diagram of the working model of the CS Ti-SiO_2 TENG. The residual charges decreased more rapidly with the increase in the temperature, and it is interesting to note that they started to decrease more rapidly once the temperature was higher than 533 K.

It is worthwhile to note that the aforementioned experiments are the results after holding the TENG at different temperatures for five minutes. In order to further systematically explore the effect of high temperature on Q_{SC}, long-term measurements were conducted on the TENG under various temperatures. Figure 1.1d shows long-term charge decay under high temperatures, which indicates that the increase in temperature facilitates charge decay. It also reveals that the Q_{SC} response is analogous to exponential decay under high temperatures. In addition, taking the temperature of 503 K as an example, all of Q_{SC}, V_{OC}, and short-circuit current I_{SC} share the same decay characteristics, which feature a slow-fast-slow trend in decay speed.

Ruckdeschel and Hunter studied the CE of Al_2O_3-glass in the range of 293–393 K and observed the charge decay at high temperatures [28]. However, they only attributed this phenomenon to the thermal desorption of water on the Al_2O_3 surface. Here, since the Q_{SC} decay is analogous to exponential decay at higher temperatures, it is assumed that they may be consistent with the electron thermionic emission model, which is always applied for charge transport through Schottky diodes [29, 30]. Thus, the measured Q_{SC} values are fitted according to the thermionic emission equation [31, 32]:

$$J = \lambda A_0 T^2 e^{\frac{W}{kT}} \left[e^{\frac{\Delta W}{kT}} - 1 \right] \tag{1.1}$$

where J is current density, λ is the material-specific correction factor, A_0 is Richardson constant of a free electron, T is temperature, W is height of the potential barrier, k is Boltzmann constant, and ΔW is the potential barrier height variation due to the surface electric field E. Such potential barrier height W might be related to the work function of materials [12]. Since $E \propto \frac{\sigma}{\epsilon_0} \propto Q_{SC}$, we may assume that $\Delta W = \lambda_1 Q_{SC}/\lambda$. ($\lambda_1$ is a constant). When $\Delta W \ll kT$, $e^{\frac{\Delta W}{kT}} - 1 \approx \frac{\Delta W}{kT}$, then

$$J = \frac{\lambda_1 A_0}{k} T e^{\frac{eV}{kT}} Q_{SC} \tag{1.2}$$

or equivalently:

$$\ln\left(\frac{J}{A_0 T}\right) = -\frac{eV}{kT} + \ln\left(\frac{\lambda_1}{k} Q_{SC}\right) \tag{1.3}$$

where e is the electronic charge. By assuming $J = \frac{1}{A}\frac{dQ_{SC}}{dt} = SQ_{SC}$, where A is the surface area:

$$Q_{SC} = e^{-SAt}Q_{SC0} \tag{1.4}$$

where Q_{SC0} is the initial value of Q_{SC}. According to Equation (1.4), Q_{SC} follows an exponential decay during thermionic emission. For tested metal/Kapton pairs, such exponential decay relations are shown in Figure 1.2a,d,g. Evolution of the measured Q_{SC} in the Al/Kapton pair at different temperatures was summarized in Figure 1.2b, similar to that of Ti/Kapton and SLS/Kapton pairs as shown in Figure 1.2e,h. Residual ratios of metal/Kapton pairs at different temperatures are summarized in Figure S2, where around 60% Q_{SC} remained on the surface with T of 420 K, but rapidly

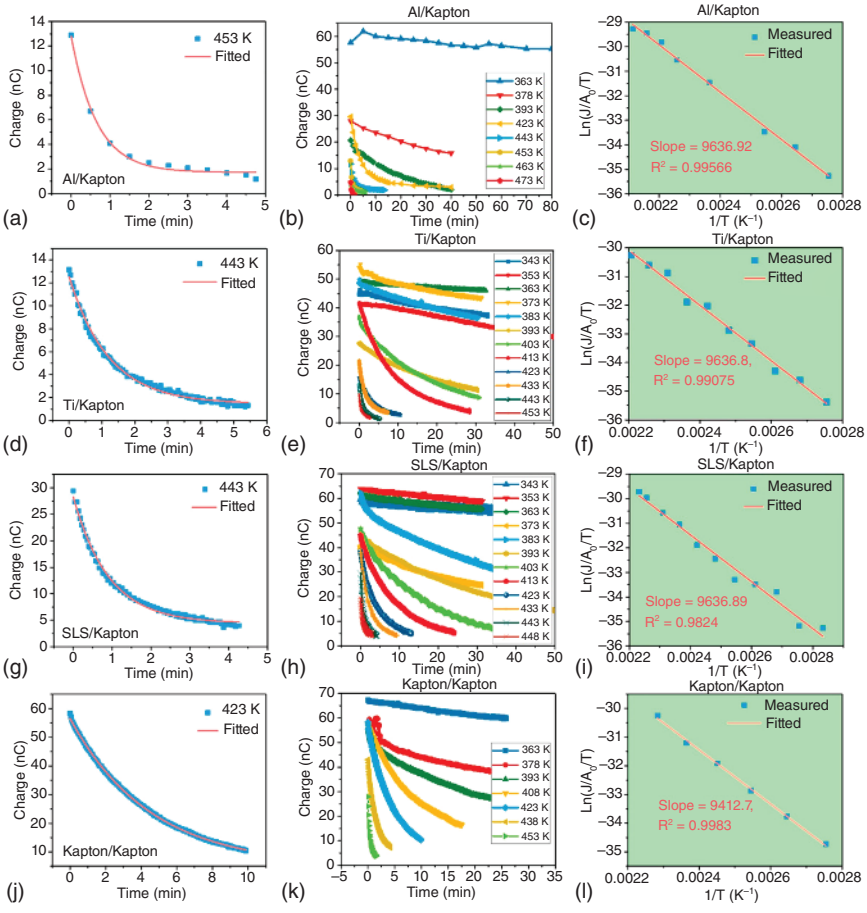

Figure 1.2 Results of metal/Kapton and Kapton/Kapton tribo-pairs. The measured (dots) and fitted (line) Q_{SC} as a function of the time at various temperatures, evolution of Q_{SC} with time at different temperatures, plots of $\ln(J/A_0/T)$ against $1/T$ with measured results in dots and linear fitted results in line, for (a–c) Al/Kapton; (d–f) Ti/Kapton; (g–i) SLS/Kapton; (j–l) Kapton/Kapton, respectively. Fitted slope of the plots of $\ln(J/A_0/T)$ against $1/T$ and the R^2 are marked next to the line. Source: Reproduced with permission of [33], 2020 © Elsevier.

decreased to 20% when T reached 450 K. Plots of $\ln(J/A_0/T)$ against $1/T$ with measured results in dots for Al/Kapton, Ti/Kapton, and SLS/Kapton pairs were shown in Figure 1.2c,f,i, respectively. Slopes of the fitted lines of $\ln(J/A_0/T)$ against $1/T$ and the coefficients of determination R^2 were marked next to the line. It should be noted that all slopes for metal/Kapton pairs with different metals are around 9600, with very little variation. This reflects that the material for thermionic emission is identical for these pairs, which should be Kapton. To confirm this conclusion, the tribo-pair of Kapton/Kapton was employed in experiments to rule out the potential influence of metals and served as a reference experiment. The exponential decay with fitted curves at 423 K, evolution of Q_{SC} with time at different temperatures, and plots of $\ln(J/A_0/T)$ against $1/T$ for the Kapton/Kapton pair were shown in Figure 1.2j–l, respectively. The slope in Figure 1.2l is similar to that of metal/Kapton pairs, verifying Kapton as the only possible thermionic emission material in metal/Kapton pairs. The extracted W of 0.82745 ± 0.0173 eV from these tribo-pairs should be that of the Kapton surface.

1.3 Material-Dependent Charge Transfer Mechanism and Model

According to the previous results of metal/Kapton in Figure 1.2, thermionic emission electrons carried by Kapton as material B were originally transferred from metals as material A, confirming the electron transfer dominant mechanism. To further study the dominant charge transfer mechanism during CE, experiments of nine other metal/polymer pairs were conducted, where Al, Ti, and SLS were applied as the positive surfaces to contact with three polymers of fluorinated ethylene propylene (FEP), polycarbonate (PC), and polyether ether ketone (PEEK). These polymers were employed due to their relatively high working temperature limits, which are all around or over 473 K. Residual ratio of metal/FEP pairs gradually decreased with temperature increase, similar to that of metal/Kapton pairs. Such trends were quite different in residual ratio of metal/PC and metal/PEEK pairs due to the effects of glass transition in PC and PEEK, indicating possibly different W at the temperature below (part I) and above (part II) the glass transition, as marked W_I and W_{II}. Thus, analysis was conducted separately for temperatures below and above the glass transition of each polymer. Considering the surface properties of polymers are usually complicated during the glass transition, the data collected during the glass transition temperature range was not analyzed. We may conclude from the results in Table 1.1 that W extracted from metal/polymer pairs is usually consistent with that of negative polymers, as measured from identical polymer/polymer pairs.

Besides metal/polymer pairs, studies about four polymer/polymer pairs were conducted, with results shown in Table 1.1. For polymer/polymer pairs, the extracted W is more complicated, which is all quite different from that of material B, and besides only a few of them are similar to that of material A. It should be noticed that W extracted from the Kapton/PC pair is between that of Kapton and PC for both temperature ranges (Parts I & II), indicating the co-existence of both electron transfer

Table 1.1 Summary and comparison of different tribo-pairs.

Tribo-pairs (Positive/Negative)		Part I ($T < T_g$)		Part II ($T > T_g$)	
		Slope	W_I (eV)	Slope	W_{II} (eV)
Metal/Kapton	Al/Kapton	9803.2	0.844778	N/A	N/A
	Ti/Kapton	9649.8	0.831559		
	SLS/Kapton	9542.9	0.822347		
Metal/PC	Al/PC	3763	0.324271	20 097	1.7318
	Ti/PC	3562.5	0.306994	19 498	1.6802
	SLS/PC	3210.3	0.276639	18 773.6	1.6178
Metal/PEEK	Al/PEEK	6563.2	0.565575	24 600.1	2.1199
	Ti/PEEK	5288.5	0.455729	26 695	2.3004
	SLS/PEEK	6819	0.587618	24 258	2.0904
Metal/FEP	Al/FEP			6737.2	0.5806
	Ti/FEP	N/A	N/A	6477.8	0.5582
	SLS/FEP			6368.2	0.5488
Polymer/polymer	Kapton/FEP	N/A	N/A	3772.3	0.3251
	Kapton/PC	6393.7	0.550969	15 642.3	1.3480
	Kapton/Kapton	9412.7	0.811127	N/A	N/A
	PEEK/PC	6886.65	0.593448	24 967.65	2.1516
	PC/FEP	3520	0.303331281	11519	0.9926
	FEP/FEP	N/A	N/A	6234.5	0.5372

and material/ion transfer mechanisms according to Figure 1.1d. Similar trends can be observed in PC/FEP pair, where W_{II} of PC/FEP pair is between PC and FEP and W_I extracted is similar to that of PC. Additionally, W_{II} extracted from Kapton/FEP was 0.3251 eV, which is lower than that of both Kapton and FEP, indicating possibly varied surface chemical status. W_I and W_{II} from PEEK/PC were always far away from that of PC as the negative material but similar to W_I and W_{II} of PEEK, respectively, indicating a possibly material transfer mechanism. Thus, it can be concluded that the W extracted from polymer/polymer pairs is usually different from that of negative polymers, indicating that material/ion transfer, electron transfer, and even chemical reactions may co-exist in CE of polymer/polymer pairs. And besides, the dominant charge transfer mechanism in CE is highly dependent on the type of material pairs.

The model to illustrate the material-dependent charge transfer mechanisms in CE was established in this work. As illustrated in Figure 1.3a, CE in metal/dielectric pairs usually follows electron transfer dominant mechanism, as demonstrated in this article as well as numerous previous studies. Figure 1.3b shows the potential CE mechanisms of dielectric/dielectric pairs. When the pairs are contacted together, electron transfer along with possibly ion/material transfer happens simultaneously,

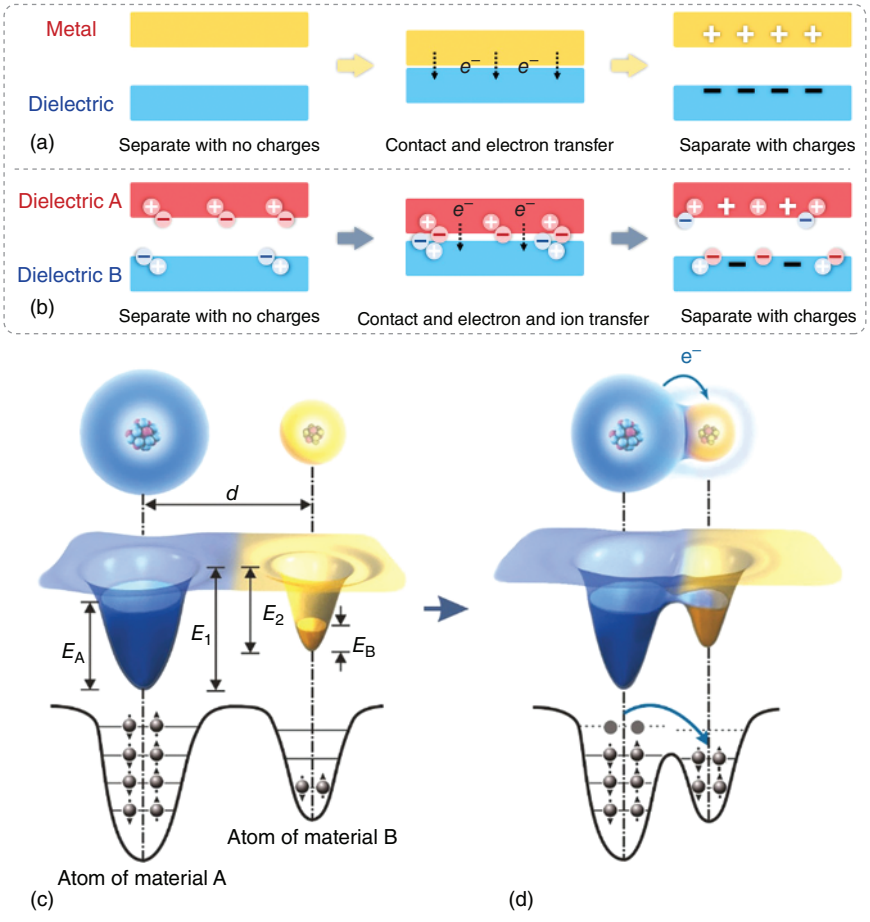

Figure 1.3 Mechanisms and model for contact electrification. (a) Illustration for electron transfer dominant mechanism in CE of metal/dielectric pairs. (b) Illustration for charge transfer mechanisms in CE of dielectric/dielectric pairs. Source: Reproduced with permission of [33], 2020 © Elsevier. Schematic of the electron cloud and potential energy profile (3D and 2D) of two atoms belonging to two materials A and B, respectively, when they are: (c) before contact and (d) in contact. Source: Reproduced with permission of [11], 2018 © John Wiley & Sons.

while the ratio of transferred charge contributed by each part varies a lot in different pairs, which is still waiting for further studies. After separation, both negative and positive charges may co-exist on the surface, consistent with the mosaic patterns observed before, while the net charge of a certain material may be either positive or negative. This model is also consistent with the covalent bond cleavage mechanism proposed previously [26, 34, 35], where the cleavage between interfacial bonds may induce electron transfer while that within a certain material may contribute to material/ion transfer.

To explain the mechanism of electron transfer, an electron cloud/potential model based on fundamental electron cloud interaction is proposed to explain all types of

CE phenomena for general materials (Figure 1.3c). Here, the electron clouds are formed by electrons that are spatially localized within specific atoms or molecules, and occupying specific atomic or molecular orbitals. An atom can be represented by a potential well in which the outer shell electrons are loosely bounded, forming an electron cloud of the atom or molecule. As shown in Figure 1.3c, d is the distance between electron clouds, E_A and E_B are the occupied energy levels of electrons in materials A and B, and E_1 and E_2 are the required potential energies for electrons to escape from the surfaces of materials A and B, respectively. E_A and E_B are, respectively, smaller than E_1 and E_2. Before the contact of the two materials, the electrons cannot transfer due to the local trapping effect of the potential wells. When material A contacts with material B, the electron clouds overlap due to the "screening" between the two materials introduced in physical contact, and the initial single potential well becomes asymmetric double-well potential and then the electron could hop from material A to material B (Figure 1.3d). Later on, Li et al. discovered the interface interatomic electron transition as induced by photon emission in CE, which confirms the existence of electron transfer in CE [36].

Although previous studies demonstrated that electron transfer is dominant in metal/polymer CE, the complicated mechanism of polymer/polymer CE remains unclear. To address this issue, a quantified model was proposed to investigate the CE, with the contribution ratios from different charge transfer mechanisms identified for different polymers. Since the potential barrier height Φ is affected by the electric field, different charge transfer mechanisms can be distinguished by the polarity of the charge transfer and the corresponding emission materials [37]. Considering the random breakage of chemical bonds of both surfaces, the transferred materials were found to usually include both positive and negative charges. Additionally, considering the different electron affinity of local atoms in molecular chain, the electron transfer was also bidirectional, and thus the polymer/polymer CE model with six potential mechanisms was established. A quantified model for calculating the contribution ratios of different charge transfer mechanisms was thus derived, and the contribution ratios were calculated. These contribution ratios were usually larger than 1, indicating that the total generated charge in CE is actually much larger than the net surface charge, which is also consistent with the previous studies. The relationship between the positive/negative charge generation ratio and the relative wear rate ratio, as well as the relationship between the relative potential barrier height and the relative wear rate ratio, were investigated, further confirming the material-dependent CE mechanism in polymer/polymer CE.

1.4 Liquid–Solid Contact Electrification Mechanism

CE may actually happen in all possible interfaces, including not only all types of solid–solid interfaces, but also liquid–solid [38–40], liquid–liquid [41–43], and even potentially solid–gas or liquid–gas interfaces [44]. Specifically, as compared to CE in solid–solid interfaces, CE in liquid–solid interfaces (LSI) show advantages of low friction (for liquid with low viscosity), minimum wearing, and high fluidity, with

high potential applications in irregular energy harvesting [40]. Considering the potential of chemical reactions and physical processes, other potential applications of LSI include electrochemistry [45, 46], catalysis [47, 48], electrowetting [49, 50], etc., which attract broad attention from scientists and industry. However, the mechanism of CE in LSI still requires further systematic studies.

Usually, the charge transfer in LSI is believed to be related to the formation of the electric double-layer (EDL), which indicates that the ions from liquid attracted to solid surface dominate the charge distribution in LSI [51]. Such ions were distributed in a Stern layer in which ions were adsorbed next to the solid surface and a diffuse layer where the ion concentration decays with the distance to the solid surface [52]. However, the formation of EDL could be just a result instead of reason for the charge transfer. Even though the EDL was formed by ions, there is still not enough evidence to demonstrate that these ions originate from ion transfer. In fact, it was theoretically calculated that in deionized (DI) water, the ion density may not be able to provide enough ions to obtain observed charge density in LSI [53].

Lin et al. demonstrate a new method to reveal the origin of the charge in CE of LSI [54]. With a droplet of liquid drops on the surface of solid material, both ion and electron transfers may happen on the interface to transfer charge. If the high temperature was applied after the droplet was removed from the surface, thermionic emission of electrons will happen, which is similar to the process in solid–solid interface [11]. However, the thermionic emission of ions is usually quite difficult, considering the high potential barrier height for ions (8.5 eV for OH^- and 20 eV for H^+ on SiO_2 surface [55, 56]). As a comparison, the potential barrier height for electrons is usually <2.5 eV as shown in Table 1.1. Therefore, the electron will be emitted, leaving the residue charge due to ions, as shown in Figure 1.4a. Through Kelvin probe force microscopy (KPFM) equipped in atomic force microscope (AFM), the variation of the surface charge density can be monitored, as shown in Figure 1.4b. The droplet-charging and thermionic-emission processes are repeated many times as shown in Figure 1.4c, while the residue charge due to ions (red dots) increases gradually until saturation at around $-800\,\mu C/m^2$. It should be noted that most of such charge transfer was initiated by electrons, which can already achieve around $-800\,\mu C/m^2$ in the first cycle, and then more charge was transferred to more ions in following cycles. In other words, the charge transfer in CE of LSI was mostly initiated by electron transfer at the beginning, while ion accumulation on the surface becomes a stable status of charge in LSI. Similar results were also obtained in other experimental and theoretical studies [53, 57].

Therefore, as summarized by Prof. Zhong Lin Wang, the CE in LSI follows a "two-step" formation process with a hybrid EDL model [58]. As shown in Figure 1.5a, the first step of CE in LSI is similar to that in solid–solid interface, in which the electron transfer happens while the electron clouds of solid interface and liquid molecules overlap due to liquid pressures and thermal effects. The transferred electrons may remain in the charged solid surface due to the potential barrier height, as the very beginning electron transfer step to initiate the CE process. As shown in Figure 1.5b, in the second step, the ions in the liquid are attracted electrostatically to the LSI interface to form EDL. Such a migration of ions from

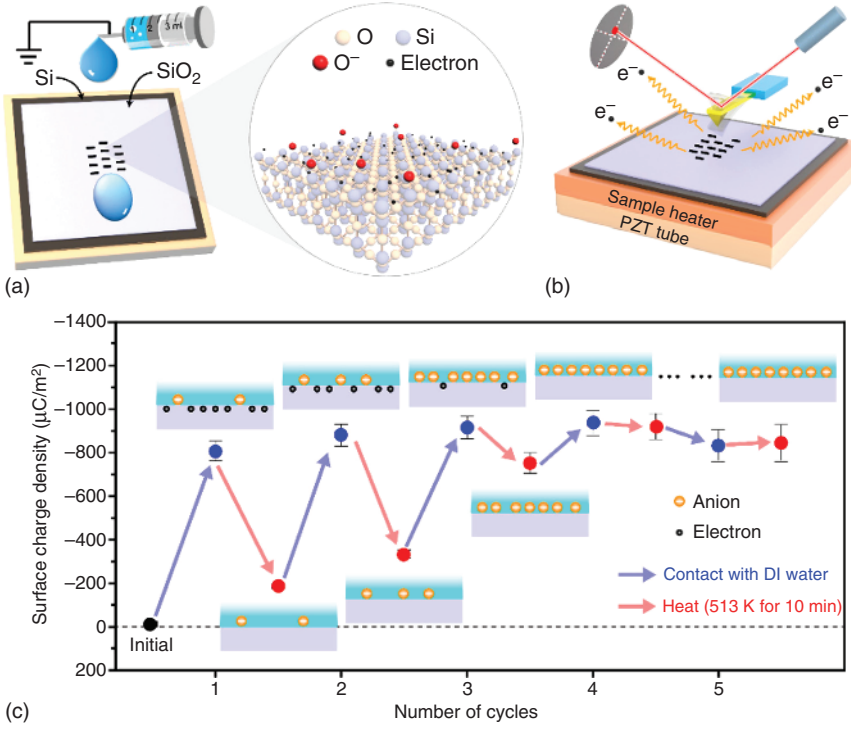

Figure 1.4 The experiment by Lin et al. to determine the charge transfer mechanism in LSI. (a) the experiment step and ion/electron formation in LSI. (b) the test method by KPFM after thermionic emission. (c) The tested charge density after repeated DI water contact and thermionic emission. Source: Reproduced with permission of [54], 2020 © Springer Nature.

liquid body to the interface may also facilitate the ionization reaction, which already exists in the liquid such as water, which further facilitates the formation of EDL. In this hybrid EDL model, the charge transfer process was initiated in the first step and dominated by electron transfer. The ion accumulation in EDL formation in the second step is just like a result of electron-dominated charge transfer. Different from solid–solid interface CE, we may assume the material transfer based on wearing is minimal in LSI interface.

1.5 Environmental and Material Effects on Charge Transfer

As a long-term mysterious phenomenon with debate over centuries, the CE mechanism still requires further explorations, which is due to the complexity brought by many impact factors. Typically, environmental factors such as temperature, humidity, stress/strain status, and atmosphere as well as material factors such as surface functional groups and strain statues, highly affect the CE process. Here, we summarized several recent studies in these aspects.

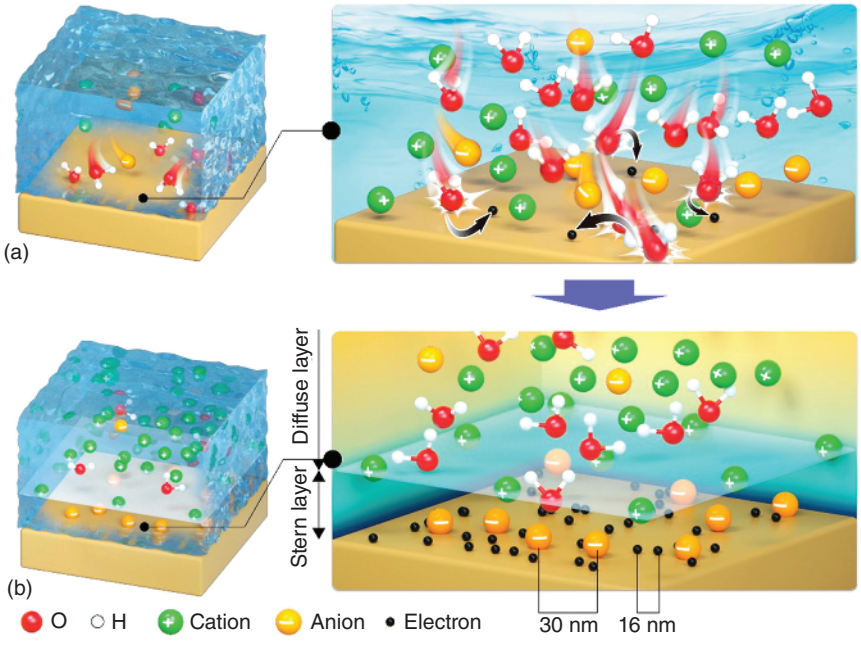

Figure 1.5 The hybrid EDL model with the "two-step" formation process for CE in LSI. (a) The electron transfer in the first step. (b) the EDL formation due to ion migration and redistribution. Source: Reproduced with permission of [44], 2022 © American Chemical Society.

1.5.1 Temperature Effect on the CE

As stated above, high temperature may facilitate the thermionic emission of electrons, as an experimental tool to reveal the CE mechanism, and in the meanwhile, it is also a pathway to release triboelectric charge, which may limit the application scenario of triboelectricity. The TENG used in previous studies is mainly based on CS motions, in which the two triboelectric surfaces are separated mostly. It has been discovered that the charge decay during contact status is much slower than that in separation status, which indicates that more charges can be kept at contact status [11]. Therefore, Wang et al. demonstrated sliding-based CE to generate more charge in high temperatures [59]. It has been discovered that sliding-based CE can facilitate CE charge transfer even in the highest temperature tested. Such a CE mechanism may comprehensively involve surface charge transfer, thermionic emission, and surface contact area changes. Based on sliding CE, Xu et al. developed the preannealing strategy to further raise the working temperature of CE, to be up to 673 K [60]. The mechanism of preannealing strategy to promote charge transfer is attributed to the atomic thermal vibration, which increases with the temperature significantly and partially balances the thermionic emission. Such annealing strategy may even change the polarity of the triboelectric charges in some materials, as carefully examined by KPFM [61]. The annealing strategy may also be unevenly applied on both sides or only on one side, which may facilitate the electron transfer from

the heated side to the unheated side, due to thermionic emission of electrons [62]. Such an effect may be used to generate and modify triboelectric charge on purpose, even in identical material pairs, considering the unevenly heated areas in contact surfaces due to frictional heat.

1.5.2 Impact of Material Surface

As an interface effect, the characteristics of CE or triboelectric effect are strongly related to the material surface. The triboelectric series, as the empirical sequence of triboelectric polarity, was usually used to select and compare triboelectric materials qualitatively. Zou et al. developed a quantitative method to understand the triboelectric series by characterizing the triboelectric charge density (TECD) as a material "gene" [63, 64]. In the meanwhile, surface of materials also plays key roles in CE. In the past decade, the method of modifying surface to promote TECD has been intensively investigated, including chemical modification method [65–67] and introduction of surface micro-/nanostructures [68–70]. However, more systematic studies are still required to quantify the promotion effect of surface functional groups.

Li et al. demonstrated that the electron-withdrawing (EW) ability of the functional groups is the key to determining their polarity and resulting TECD [71]. In various functional groups, the −F group shows the best EW ability, and increase of the −F groups can greatly enhance the negative TECD, which explains why polymers that are fully fluorinated (such as FEP and polytetrafluoroethylene, PTFE) demonstrate the best TECD compared to other common polymers. The EW ability for other common functional groups is ranked as $-CH_3 < -H < -OH < -Cl < -F$. Besides, it was discovered that unsaturated groups can enhance the EW of fluorinated polymers, such as $-CF_2{=}CF_2-$ and $-CF{\equiv}CF-$, which may be introduced to the original fluorinated polymers through thin firm sputtering, UV-ozone treatment, etc. In the meanwhile, the density of surface states (DOSS) may also contribute to the resulting TECD [72]. A model based on DOSS was proposed to explain the abnormal TECD generation between ternary materials, with an experimental method established to characterize DOSS of materials. Through this DOSS model, it can be predicted that TECD of FEP may achieve $\sim 560\,\mu C/m^2$, which is close to the reported maximum values. These studies may inspire a more complete mechanism model for CE and TECD in the near future.

1.5.3 Stress/Strain States and Others

Besides the chemical composition of the material surface, the surface stress or strain states may also impact the TECD. However, even for identical material pairs in contact, CE may also happen. Xu et al. demonstrated that the charge transfer is also related to the curvature of surfaces, while positive curvature tends to take negative charge and negative curvature tends to take positive charge [73]. The mechanism of CE between the curved surfaces may be attributed to the shift of occupied level of surface states. In light of that, mutual CE may even happen between any identical material pairs in contact considering the surface roughness,

which may result in uneven stress/strain distribution on the surface. This discovery may explain the mosaic distribution of triboelectric charge [22]. Furthermore, the applied stress/strain can also vary the electron transfer amount during CE, which may be contributed by the induced flexoelectricity [74].

For some stretchable polymer materials, the crystallization level may be induced by strain, which can greatly impact the band diagram. Liu et al. demonstrated that strain-induced crystallization can shift the position of polymers in triboelectric series, and even induce polarity reversal of TECD [75]. With the crystallization process, the electron cloud on the surface can be totally redistributed, which can greatly impact the CE process by assuming the electron-dominated electron-cloud-potential-well model. CE can also be promoted by UV light, as attributed to photoexcitation effect on electrons [15, 76], which demonstrated the existence of threshold photon energy to assist electrons to overcome the potential barrier heights. The TECD can even be modified by atmosphere, especially the oxygen atmosphere, which may both impact the DOSS and occupied energy levels [77].

1.6 Potential Applications

When two different materials or surfaces are in physical contact or sliding against one another, charges will be transferred from one surface to the other, making them positively or negatively charged, respectively. This is the triboelectric effect (also called triboelectrification or CE) well-known for thousands of years, which was first recorded by Thales of Miletus (c. 624–546 BC), an ancient Greek philosopher. Understanding and discovering methods to tailor the triboelectric effect by controlling the surface charge density will benefit a number of applications. As examples:

- *Prevention of electrostatic damage (ESD)*: The electrostatic charge produced by the triboelectric effect may cause sparks which can ignite flammable materials or vapors, interfering in the operation of electronics in the household, workplace, and societal infrastructures including public transportation, aircraft and spacecraft. It has been reported that related losses in the electronics industry are up to **US$5 billion**. (https://www.durablecorp.com/the-costs-of-esd-damage) Therefore, these industries would benefit from the ability to downregulate or decrease the triboelectric effect.
- *Power generation*: TENG is an emerging technology for low-frequency energy harvesting with demonstrated advantages of being lightweight, facile fabrication, high performance, and low cost [78]. It has been predicted that TENG and the resulting applications will be a **US$480 million market** by 2028 (https://www.idtechex.com/en/research-report/triboelectric-energy-harvesting-teng-2018-2028/577). As indicated by the TENG figure-of-merit (FOM) developed by the PI, TECD is the key parameter to maximize output performance [38]. Therefore, these applications would require that the triboelectric effect could be upregulated, maximized, or increased.

- *High-voltage applications*: For applications which require high-voltage input, such as the TENG-triggered electrospray for mass spectrometry (MS) demonstrated by the PI, quantitatively controlled charge generation is critical to achieving nanocoulomb level and ultrasensitive chemical analysis [79]. Similar research conducted by the PI includes field emission of electrons [78], and microplasma generation [80]. Here, the triboelectric effect should be tailored precisely according to the applications.
- *Self-powered wireless solution through tribophotonics*: Tribophotonics is coupling of triboelectricity as a self-powered solution and photonics as a wireless transmission solution, which was proposed in recent years [81]. The developed technologies under tribophotonics include tribo-induced EM-wave generation (TIEG), tribo-induced light propagation tuning (TILPT), tribo-induced electroluminescence (TIEL), and tribo-assisted spectrometry (TAS), which was detailed in Chapter 9. As induced by photon emission from CE, Li et al. also proposed CE-induced interface photon emission spectroscopy (CEIIPES), which can be considered a new type of TAS, and may be expanded as a new self-powered spectroscopy tool [36].

1.7 Summary

This chapter summarized the studies on CE mechanisms in recent years, as facilitated by the emerging field of TENG. Through experiments based on thermionic emission, intensive studies have been conducted on charge transfer mechanisms, with universal existence of electron transfer confirmed in CE through various studies. An electron-cloud-potential-well model was established, as key model for CE studies. In the meanwhile, the contributions from material transfer and ion transfer were studied in solid–solid interface and LSI CEs, respectively. The impacts of materials, environment, stress/strain, etc., were investigated, which greatly improved our understanding and provided charge modification tools for CE. It is expected that a more detailed CE mechanism will be revealed in the near future considering the intensive studies in recent years.

References

1 Wu, C., Wang, A.C., Ding, W. et al. (2019). Triboelectric nanogenerator: a foundation of the energy for the new era. *Adv. Energy Mater.* 9 (1): 1802906.
2 Hinchet, R., Yoon, H.-J., Ryu, H. et al. (2019). Transcutaneous ultrasound energy harvesting using capacitive triboelectric technology. *Science* 365 (6452): 491–494.
3 Zhu, G., Pan, C., Guo, W. et al. (2012). Triboelectric-generator-driven pulse electrodeposition for micropatterning. *Nano Lett.* 12 (9): 4960–4965.
4 Lebedev, M. and Akedo, J. (2002). What thickness of the piezoelectric layer with high breakdown voltage is required for the microactuator? *Jpn. J. Appl. Phys.* 41 (5B): 3344–3347.

5 Wang, J., Wu, C., Dai, Y. et al. (2017). Achieving ultrahigh triboelectric charge density for efficient energy harvesting. *Nat. Commun.* 8 (1): 88.

6 Lowell, J. and Rose-Innes, A.C. (2006). Contact electrification. *Adv. Phys.* 29 (6): 947–1023.

7 Liu, C. and Bard, A.J. (2008). Electrostatic electrochemistry at insulators. *Nat. Mater.* 7 (6): 505–509.

8 Liu, C.Y. and Bard, A.J. (2009). Chemical redox reactions induced by cryptoelectrons on a PMMA surface. *J. Am. Chem. Soc.* 131 (18): 6397–6401.

9 Liu, C.Y. and Bard, A.J. (2009). Electrons on dielectrics and contact electrification. *Chem. Phys. Lett.* 480 (4–6): 145–156.

10 Liu, C.-Y. and Bard, A.J. (2010). Electrostatic electrochemistry: nylon and polyethylene systems. *Chem. Phys. Lett.* 485 (1–3): 231–234.

11 Xu, C., Zi, Y., Wang, A.C. et al. (2018). On the electron-transfer mechanism in the contact-electrification effect. *Adv. Mater.* 30 (15): e1706790.

12 Xu, C., Zhang, B., Wang, A.C. et al. (2019). Effects of metal work function and contact potential difference on electron thermionic emission in contact electrification. *Adv. Funct. Mater.* 29 (29): 1903142.

13 Lin, S., Xu, L., Xu, C. et al. (2019). Electron transfer in nanoscale contact electrification: effect of temperature in the metal-dielectric case. *Adv. Mater.* 31 (17): e1808197.

14 Zhang, S.L., Xu, M., Zhang, C. et al. (2018). Rationally designed sea snake structure based triboelectric nanogenerators for effectively and efficiently harvesting ocean wave energy with minimized water screening effect. *Nano Energy* 48: 421–429.

15 Lin, S., Xu, L., Zhu, L. et al. (2019). Electron transfer in nanoscale contact electrification: photon excitation effect. *Adv. Mater.* 31 (27): e1901418.

16 Zhou, Y.S., Wang, S., Yang, Y. et al. (2014). Manipulating nanoscale contact electrification by an applied electric field. *Nano Lett.* 14 (3): 1567–1572.

17 Li, S., Zhou, Y., Zi, Y. et al. (2016). Excluding contact electrification in surface potential measurement using kelvin probe force microscopy. *ACS Nano* 10 (2): 2528–2535.

18 Wiles, J.A., Grzybowski, B.A., Winkleman, A., and Whitesides, G.M. (2003). A tool for studying contact electrification in systems comprising metals and insulating polymers. *Anal. Chem.* 75 (18): 4859–4867.

19 Thomas, S.W. 3rd, Vella, S.J., Kaufman, G.K., and Whitesides, G.M. (2008). Patterns of electrostatic charge and discharge in contact electrification. *Angew. Chem. Int. Ed.* 47 (35): 6654–6656.

20 McCarty, L.S. and Whitesides, G.M. (2008). Electrostatic charging due to separation of ions at interfaces: contact electrification of ionic electrets. *Angew. Chem. Int. Ed.* 47 (12): 2188–2207.

21 Thomas, S.W. 3rd, Vella, S.J., Dickey, M.D. et al. (2009). Controlling the kinetics of contact electrification with patterned surfaces. *J. Am. Chem. Soc.* 131 (25): 8746–8747.

22 Baytekin, H.T., Patashinski, A.Z., Branicki, M. et al. (2011). The mosaic of surface charge in contact electrification. *Science* 333 (6040): 308–312.

23 Baytekin, B., Baytekin, H.T., and Grzybowski, B.A. (2012). What really drives chemical reactions on contact charged surfaces? *J. Am. Chem. Soc.* 134 (17): 7223–7226.

24 Baytekin, H.T., Baytekin, B., Incorvati, J.T., and Grzybowski, B.A. (2012). Material transfer and polarity reversal in contact charging. *Angew. Chem. Int. Ed.* 51 (20): 4843–4847.

25 Siek, M., Adamkiewicz, W., Sobolev, Y.I., and Grzybowski, B.A. (2018). The influence of distant substrates on the outcome of contact electrification. *Angew. Chem. Int. Ed.* 57 (47): 15379–15383.

26 Pezzotti, G., Camara, C., Marin, E. et al. (2019). Physical chemistry insights into surface charge phenomena during frictional coupling in triboelectric X-ray sources. *J. Mater. Chem. C* 7 (25): 7708–7724.

27 Šutka, A., Mālnieks, K., Lapčinskis, L. et al. (2019). The role of intermolecular forces in contact electrification on polymer surfaces and triboelectric nanogenerators. *Energy Environ. Sci.* 12 (8): 2417–2421.

28 Ruckdeschel, F.R. and Hunter, L.P. (2008). Contact electrification between insulators: phenomenological aspects. *J. Appl. Phys.* 46 (10): 4416–4430.

29 Crowell, C.R. and Sze, S.M. (1966). Current transport in metal-semiconductor barriers. *Solid State Electron.* 9 (11): 1035–1048.

30 Ravinandan, M., Rao, P.K., and Rajagopal Reddy, V. (2009). Analysis of the current–voltage characteristics of the Pd/Au Schottky structure on n-type GaN in a wide temperature range. *Semicond. Sci. Technol.* 24 (3): 035004.

31 Crowell, C.R. (1965). The Richardson constant for thermionic emission in Schottky barrier diodes. *Solid State Electron.* 8 (4): 395–399.

32 Racko, J., Grmanová, A., and Breza, J. (1996). Extended thermionic emission-diffusion theory of charge transport through a Schottky diode. *Solid State Electron.* 39 (3): 391–397.

33 Xia, X., Wang, H., Guo, H. et al. (2020). On the material-dependent charge transfer mechanism of the contact electrification. *Nano Energy* 78: 105343.

34 Li, A., Liu, Y., and Szlufarska, I. (2014). Effects of interfacial bonding on friction and Wear at silica/silica interfaces. *Tribol. Lett.* 56 (3): 481–490.

35 Zhang, J., Rogers, F.J.M., Darwish, N. et al. (2019). Electrochemistry on tribocharged polymers is governed by the stability of surface charges rather than charging magnitude. *J. Am. Chem. Soc.* 141 (14): 5863–5870.

36 Li, D., Xu, C., Liao, Y. et al. (2021). Interface inter-atomic electron-transition induced photon emission in contact-electrification. *Sci. Adv.* 7 (39): eabj0349.

37 Xia, X., Wang, H., and Zi, Y. (2022). Field-assisted thermionic emission toward quantitative modeling of charge-transfer mechanisms in contact electrification. *SmartMat* 3 (4): 619–631.

38 Zi, Y.L., Niu, S.M., Wang, J. et al. (2015). Standards and figure-of-merits for quantifying the performance of triboelectric nanogenerators. *Nat. Commun.* 6: 8376.

39 Xu, W., Zheng, H., Liu, Y. et al. (2020). A droplet-based electricity generator with high instantaneous power density. *Nature* 578 (7795): 392–396.

40 Wu, H., Wang, Z., and Zi, Y. (2021). Multi-mode water-tube-based triboelectric nanogenerator designed for low-frequency energy harvesting with ultrahigh volumetric charge density. *Adv. Energy. Mater.* 11 (16): 2100038.

41 Jiang, P., Zhang, L., Guo, H. et al. (2019). Signal output of triboelectric nanogenerator at oil–water–solid multiphase interfaces and its application for dual-signal chemical sensing. *Adv. Mater.* 31 (39): 1902793.

42 Wang, P., Zhang, S., Zhang, L. et al. (2020). Non-contact and liquid–liquid interfacing triboelectric nanogenerator for self-powered water/liquid level sensing. *Nano Energy* 72: 104703.

43 Nie, J., Wang, Z., Ren, Z. et al. (2019). Power generation from the interaction of a liquid droplet and a liquid membrane. *Nat. Commun.* 10 (1): 2264.

44 Lin, S., Chen, X., and Wang, Z.L. (2022). Contact electrification at the liquid–solid interface. *Chem. Rev.* 122 (5): 5209–5232.

45 Magnussen, O.M. and Groß, A. (2019). Toward an atomic-scale understanding of electrochemical Interface structure and dynamics. *J. Am. Chem. Soc.* 141 (12): 4777–4790.

46 Zaera, F. (2012). Probing liquid/solid interfaces at the molecular level. *Chem. Rev.* 112 (5): 2920–2986.

47 Lee, S.H., Nedrygailov, I.I., Oh, S., and Park, J.Y. (2018). Hot electron flux at solid–liquid interfaces probed with Pt/Si catalytic nanodiodes: effects of pH during decomposition of hydrogen peroxide. *Catal. Today* 303: 282–288.

48 Tao, F. and Crozier, P.A. (2016). Atomic-scale observations of catalyst structures under reaction conditions and during catalysis. *Chem. Rev.* 116 (6): 3487–3539.

49 Wang, J., Wang, H., Li, X., and Zi, Y. (2019). Self-powered electrowetting optical switch driven by a triboelectric nanogenerator for wireless sensing. *Nano Energy* 66: 104140.

50 Li, X., Tian, H., Shao, J. et al. (2016). Decreasing the saturated contact angle in electrowetting-on-dielectrics by controlling the charge trapping at liquid–solid interfaces. *Adv. Funct. Mater.* 26 (18): 2994–3002.

51 Helmholtz, H. (1853). Ueber einige Gesetze der Vertheilung elektrischer Ströme in körperlichen Leitern mit Anwendung auf die thierisch-elektrischen Versuche. *Ann. Phys.* 165 (6): 211–233.

52 Stern, O. (1924). The theory of the electric double layer. *Electrochemistry* 30: 508.

53 Nie, J., Ren, Z., Xu, L. et al. (2020). Probing contact-electrification-induced electron and ion transfers at a liquid–solid interface. *Adv. Mater.* 32 (2): 1905696.

54 Lin, S., Xu, L., Chi Wang, A., and Wang, Z.L. (2020). Quantifying electron-transfer in liquid-solid contact electrification and the formation of electric double-layer. *Nat. Commun.* 11 (1): 399.

55 von Burg, K. and Delahay, P. (1981). Photoelectron emission spectroscopy of inorganic anions in aqueous solution. *Chem. Phys. Lett.* 78 (2): 287–290.

56 Takakuwa, Y., Niwano, M., Nogawa, M. et al. (1989). Photon-stimulated desorption of H+ ions from oxidized Si(111) surfaces. *Jpn. J. Appl. Phys.* 28 (12R): 2581.

57 Zhan, F., Wang, A.C., Xu, L. et al. (2020). Electron transfer as a liquid droplet contacting a polymer surface. *ACS Nano* 14 (12): 17565–17573.

58 Wang, Z.L. and Wang, A.C. (2019). On the origin of contact-electrification. *Mater. Today* 30: 34–51.

59 Wang, A.C., Zhang, B., Xu, C. et al. (2020). Unraveling temperature-dependent contact electrification between sliding-mode triboelectric pairs. *Adv. Funct. Mater.* 30 (12): 1909384.

60 Xu, C., Wang, A.C., Zou, H. et al. (2018). Raising the working temperature of a triboelectric nanogenerator by quenching down electron thermionic emission in contact-electrification. *Adv. Mater.* 30 (38): 1803968.

61 Zhu, Y., Lin, S., Gao, W. et al. (2021). Reversal of triboelectric charges on sol–gel oxide films annealed at different temperatures. *Appl. Phys. Lett.* 118 (24): 243902.

62 Lin, S., Xu, L., Xu, C. et al. (2019). Electron transfer in nanoscale contact electrification: effect of temperature in the metal–dielectric case. *Adv. Mater.* 31 (17): 1808197.

63 Zou, H., Guo, L., Xue, H. et al. (2020). Quantifying and understanding the triboelectric series of inorganic non-metallic materials. *Nat. Commun.* 11 (1): 2093.

64 Zou, H., Zhang, Y., Guo, L. et al. (2019). Quantifying the triboelectric series. *Nat. Commun.* 10 (1): 1427.

65 Wang, S., Zi, Y., Zhou, Y.S. et al. (2016). Molecular surface functionalization to enhance the power output of triboelectric nanogenerators. *J. Mater. Chem. A* 4 (10): 3728–3734.

66 Zhang, X.-S., Han, M.-D., Wang, R.-X. et al. (2014). High-performance triboelectric nanogenerator with enhanced energy density based on single-step fluorocarbon plasma treatment. *Nano Energy* 4: 123–131.

67 Wang, J., Li, S., Yi, F. et al. (2016). Sustainably powering wearable electronics solely by biomechanical energy. *Nat. Commun.* 7 (1): 12744.

68 Zhong, J., Zhong, Q., Fan, F. et al. (2013). Finger typing driven triboelectric nanogenerator and its use for instantaneously lighting up LEDs. *Nano Energy* 2 (4): 491–497.

69 Wang, J., Wen, Z., Zi, Y. et al. (2016). All-plastic-materials based self-charging power system composed of triboelectric nanogenerators and supercapacitors. *Adv. Funct. Mater.* 26 (7): 1070–1076.

70 Cui, N., Gu, L., Lei, Y. et al. (2016). Dynamic behavior of the triboelectric charges and structural optimization of the friction layer for a triboelectric nanogenerator. *ACS Nano* 10 (6): 6131–6138.

71 Li, S., Nie, J., Shi, Y. et al. (2020). Contributions of different functional groups to contact electrification of polymers. *Adv. Mater.* 32 (25): e2001307.

72 Xu, G., Guan, D., Fu, J. et al. (2022). Density of surface states: another key contributing factor in triboelectric charge generation. *ACS Appl. Mater. Interfaces* 14 (4): 5355–5362.

73 Xu, C., Zhang, B., Wang, A.C. et al. (2019). Contact-electrification between two identical materials: curvature effect. *ACS Nano* 13 (2): 2034–2041.

74 Lin, S., Zheng, M., Xu, L. et al. (2022). Electron transfer driven by tip-induced flexoelectricity in contact electrification. *J. Phys. D. Appl. Phys.* 55 (31): 315502.

75 Liu, Z., Li, S., Lin, S. et al. (2022). Crystallization-induced shift in a triboelectric series and even polarity reversal for elastic triboelectric materials. *Nano Lett.* 22 (10): 4074–4082.
76 Tao, X., Nie, J., Li, S. et al. (2021). Effect of photo-excitation on contact electrification at liquid–solid interface. *ACS Nano* 15 (6): 10609–10617.
77 Lin, S., Xu, L., Tang, W. et al. (2019). Electron transfer in nano-scale contact electrification: atmosphere effect on the surface states of dielectrics. *Nano Energy* 65: 103956.
78 Wang, Z.L., Lin, L., Chen, J. et al. (2016). *Triboelectric Nanogenerators*. Springer.
79 Li, A., Zi, Y., Guo, H. et al. (2017). Triboelectric nanogenerators for sensitive nano-coulomb molecular mass spectrometry. *Nat. Nanotechnol.* 12 (5): 481.
80 Cheng, J., Ding, W., Zi, Y. et al. (2018). Triboelectric microplasma powered by mechanical stimuli. *Nat. Commun.* 9 (1): 3733.
81 Wang, H., Xia, X., Fu, J. et al. (2023). A general self-powered wireless sensing solution based on triboelectric-discharge effect. *Nano Energy* 105: 107982.